Tungsten (2019) 1:306–317
https://doi.org/10.1007/s42864-020-00032-y

Tungsten
www.springer.com/42864

ORIGINAL PAPER

Improved thermochromic and photocatalytic activities of F–VO_2/Nb–TiO_2 multifunctional coating films

Anung Riapanitra[1] · Yusuke Asakura[1] · Shu Yin[1]

Received: 31 August 2019 / Revised: 29 September 2019 / Accepted: 30 September 2019 / Published online: 27 January 2020

Abstract

Multifunctional photocatalytic and thermochromic composites consisting of fluorine-doped vanadium dioxide (F–VO_2) and niobium-doped TiO_2 (NTO) were prepared by a simple physical mixing. The composites exhibited a higher thermochromic activity and nitrogen oxide (NO_x) decomposition activity than that of pristine VO_2/NTO. Both VO_2 and NTO materials were synthesized using an environmentally friendly soft chemical solvothermal/hydrothermal process, which produced NTO nanoparticles with a controllable morphology and particle size by changing the ratio of ethanol and acetic acid solvent. F–VO_2/NTO showed a better multifunctionality of thermochromic and photocatalytic activities than those of VO_2/NTO samples. The coexistence coating films showed a better effect on thermochromic and deNO_x (NO_x reduction) activity than those of double-sided films for F–VO_2/NTO samples. The best thermochromic and photocatalytic activities obtained from sample F–VO_2/NTO 60 showed the $\Delta T_{1500\ nm}$ [difference of transmittance (ΔT) at the wavelength of 1500 nm under 25 °C and 95 °C] of up to 29.5% and deNO_x activity of up to 40% at $\lambda > 290$ nm under mercury lamp irradiation. The use of F–VO_2/NTO coexistence coating films showed the appropriateness for multifunctional materials.

Keywords Nb-doped TiO_2 · VO_2(M) · Thermochromic · Photocatalytic NO_x decomposition · Multifunctional coating

1 Introduction

The mitigation of energy consumption has been a crucial research topic nowadays. Energy consumption of buildings takes a soaring account of 40% of the world total energy consumption per year [1]. Many ways are suggested to increase building efficiencies such as the use of phase-changing materials to store energy and the use of the energy-efficient window. The utilization of near-infrared (NIR) shielding materials using noble metal and doped tungsten trioxides showed merits to increase the functionality of windows [2–4]. What is equally important was the use of chromogenic materials to shield or convey NIR irradiation flexibly. The use of tungsten as electrochromic materials is developed. Meanwhile thermochromic materials are widely explored with the use of vanadium dioxide, which solely based on temperature stimuli without requirement of the electrical current to trigger the switching properties [5–10]. The unique optical property of VO_2 is the fast and reversible metal-to-semiconductor transformation (MST) [11]. This phenomenon occurs at a critical temperature of 68 °C, during which the monoclinic structure of VO_2 changes into the rutile structure. This reversible switching makes it beneficial for VO_2 to be applied as a smart thermochromic coating for windows [12, 13]. Many ways are available to prepare VO_2 which can increase its property required for smart window coating applications. The nanoparticle synthesis is an advantageous way to obtain a thin film with the excellent thermochromic performance, due to the suppression of light scattering by the decreasing particle size. On the other hand, doping was utilized to reduce the critical phase transition temperature of VO_2, among which tungsten and fluorine were the prominently used dopants [14, 15].

Photocatalytic materials such as ZnO and TiO_2 were developed as functional layers on windows [8–10]. Photocatalysis is an environmentally friendly process which is essential to advance the multifunctionality of smart windows [16]. The advantages of photocatalytic materials include the self-cleaning property, transparency, low cost, and biocompatibility [17]. TiO_2 is the most widely used photocatalytic semiconductor with the bandgap of 3.2 eV, meaning that

✉ Shu Yin
yin.shu.b5@tohoku.ac.jp

[1] Institute of Multidisciplinary Research for Advanced Materials, Tohoku University, Sendai 980-8577, Japan

it can effectively work as a photocatalyst under ultraviolet (UV) light irradiation [18]. Doping of ions in the TiO_2 lattice was performed to enhance its photocatalytic performance under visible (Vis) light irradiation. Many kinds of cations and anions such as carbon, fluorine, nitrogen, and niobium were implemented as doping for TiO_2 [19–22]. Nb-doped TiO_2 (NTO) had the benefits of the high conductivity and transparency [23], which were potential as a transparent conducting oxide for dye-sensitized solar cells (DSSC) [24, 25], photoelectrochemical [26], and photocatalysis [27, 28]. The substitution of Nb to the Ti site causes the movement of electrons to the Ti 3*d* orbital, giving NTO the ability to shield the NIR wavelength. The photocatalytic and NIR shielding properties of NTO make it be used as the potential component of composite with thermochromic VO_2 to realize multifunctional properties [29]. The VO_2/TiO_2 composites were synthesized with many procedures such as pulsed laser deposition [30, 31], electric field aerosol assisted chemical vapor deposition [32], atmospheric pressure chemical vapor deposition [33], direct current (DC) magnetron sputtering [34] and reactive magnetron sputtering [35]. These methods produced thin films with the satisfying thickness; however, they suffered from the use of expensive instruments, lower purity of monoclinic phase VO_2, and low thermochromic performance. The hydrothermal synthesis, on the other hand, offers an environmentally friendly method to produce nanoparticles and control the morphology of the product with a relatively simple and facile procedure [36]. Doping of VO_2 synthesized by the hydrothermal process was found to enhance the thermochromic property [37, 38].

In this work, fluorine-doped VO_2(M) (F–VO_2) and NTO as the components for the multifunctional composite coatings were examined with pristine VO_2 as the comparison. Fluorine doping was used to reduce the critical temperature of VO_2 MST. Anionic doping endows samples with high compatibility, and therefore similar approaches of anion doping were also widely performed in photocatalysis research [19, 39]. It is urgent to combine NTO with VO_2(M) since NTO possesses the NIR shielding property. Both NTO and VO_2(M) were synthesized using the solvothermal process to provide good control of morphology and nanosize products, preventing the light scattering at the visible range wavelength. F–VO_2 nanoparticles were synthesized by the one-step hydrothermal synthesis process, and meanwhile, NTO nanoparticles were synthesized using a water-controlled release solvothermal process (WCRSP) [36]. The concentration variation of the ethanol and acetic acid solvent is subject to the creation of the anatase phase. The composite coating films were examined under two conditions: double-sided and coexistence coating films. The preparation of coexistence and double-sided type coating films were aimed to compare the multifunctionality and compatibility of the composites with each of its constituents. In the coexistent film, the VO_2(M)/NTO or F–VO_2/NTO was mixed and cast on the same side of a glass surface; for double-sided films, the VO_2(M)/NTO or F–VO_2/NTO was cast separately in the opposite surface of the coating glass. The composite coating films of F–VO_2/NTO provide a novel approach to tune the thermochromic and photocatalytic performance for multifunctional materials.

2 Experimental

2.1 Synthesis of NTO by WCRSP

All chemical reagents used were of commercially available analytical grade and were used without further purification. The synthesis procedure was based on a previous report [40]. Niobium penta-ethoxide (0.3 mmol, Wako Pure Chemical Industries, Ltd) and titanium tetra-isopropoxide (2 mmol, Kanto Chemical Co., Inc.) were added to a mixed solvent with various concentrations of ethanol and acetic acid (60 mL). The volume ratios of ethanol and acetic acid were adjusted to 60:0, 45:15, and 35:25, respectively. Hence the sample was denoted with the amount of ethanol used in the synthesis as NTO 60, NTO 45, and NTO 35, respectively. The mixture was further stirred for 30 min before being transferred into a Teflon-sealed autoclave and heated at 240 °C for 24 h. The product was then cooled, filtrated, washed by ethanol and dried under a reduced pressure oven at 60 °C over night.

2.2 Synthesis of VO_2(M) and F–VO_2(M)

The synthesis procedure was based on the previous report [41]. Vanadium pentoxide (0.05 mmol, Kanto Chemical Co.) with a specific surface area of 24.32 m^{-2} g^{-1} and typical particle size of > 100 μm was diluted into 28 mL of H_2O. Hydrogen peroxide was added (5 mL, 30%, Kanto Chemical Co.). After an overnight stirring at 60 °C, with a speed of 600 r min^{-1}, a requisite amount of hydrazine monohydrate (Kanto chemical co.) was added. Then the mixture was stirred for 5 min. Further, the hydrothermal synthesis was performed at 490 °C for 30 min. The product was collected using centrifugation, washed using water and ethanol, and dried at a reduced pressure oven at 60 °C. For the F–VO_2 sample synthesis, a similar method was performed with the addition of NH_4F (Kanto Chemical Co.), after hydrogen peroxide was added to provide a 10 mol% of fluorine doping.

2.3 Smart coating of the composites

NTO (0.015 g) was mixed with VO_2 (0.015 g) or F–VO_2 (0.015 g) using mixture of ethanol (0.5 ml, Wako Pure Chemical Industries, Ltd) and collodion (0.5 ml, Wako Pure

Chemical Industries, Ltd) as the medium to obtain the mixture dispersion. The mixture was stirred with ZrO_2 beads (1.5 mm diameter, 5 g) for 24 h at 600 r min^{-1} and cast into the surface of a glass. For the double-sided films, a similar method was performed where each NTO (0.015 g), VO_2 or F–VO_2 (0.015 g) was dispersed in ethanol and collodion and the mixture was further stirred for 24 h at 600 r min^{-1}. The dispersion was cast using a doctor blade applicator with a thickness of 50 µm, setting onto a borosilicate glass. In the coexistent film, the VO_2(M)/NTO or F–VO_2/NTO mixture dispersion was cast on the same side of the glass surface. For double-sided films, each of the VO_2(M)/NTO or F–VO_2/NTO dispersion was separately cast in the opposite surface of the glass. The coating film was heated at 200 °C for 1 h followed by natural cooling. The specific surface area of the sample was measured by the Brunauer–Emmett–Teller (BET) method.

2.4 Characterization

The structure of the nanoparticle was examined by a transmission electron microscopy (TEM, Jeol JEM-2000 EXII). High-resolution transmission electron microscopy and selected area electron diffraction (SAED) images were obtained using a high-resolution transmission electron microscope (HRTEM, JEOL JEM-2100F). The powder X-ray diffraction (XRD) patterns were examined using an X-ray diffraction with Cu Kα radiation (XRD, Bruker D2 Phaser, $\lambda = 0.15418$ nm). The binding energy of the contained elements was confirmed via an X-ray photoelectron spectroscopy (XPS, ULVAC PHI 5600, ULVAC PHI Co., Ltd.). The transmittance of the thin films was analyzed in a wavelength range of 190-2500 nm using UV–Vis–NIR spectrophotometer (Jasco V-600, JASCO) equipped with a film heating attachment. The photocatalytic activity evaluation was performed using NO_x decomposition as a model reaction. The deNO_x photocatalytic activity was measured using a NO_x analyzer (Yanaco Co., ECL-88AO Lite). For the photocatalytic characterization, the coating film with a thickness of 50 µm was also prepared. The exposed surface was adjusted to 20 mm × 20 mm in size, and the glass was set at the bottom of a photocatalytic reactor under mercury lamp irradiation at 290 nm, which was stabilized using a chiller set at room temperature. The NO_x total concentration of the sample gas was set to 1 mg kg^{-1} using the mixture of NO (2 mg kg^{-1})/N_2 gas and compressed air. A flow rate of 200 mL min^{-1} was used to saturate the reactor chamber before the measurement. The stability of the photocatalyst was evaluated by conducting the photocatalytic reaction for six cycles.

3 Results and discussion

3.1 Characterization of NTO and evaluation of its NIR shielding and photocatalytic activities

The XRD analysis was used to determine the crystallographic structure and phase of NTO. Figure 1 shows the XRD patterns of NTO synthesized with varied ethanol and acetic acid contents. All peaks consisted of the anatase phase that matched to the reference (JCPDS 89-4921) well. Neither the trace of the rutile diffraction peak nor the niobium oxide peak can be observed. A shift to the small angle diffraction was observed, indicating that Nb^{5+} was doped into the TiO_2 lattice, due to the different radii between Ti^{4+} and Nb^{5+} and the radius of Nb^{5+} was larger (Fig. 1b). The decreasing crystallite size could be observed through the broadening at the

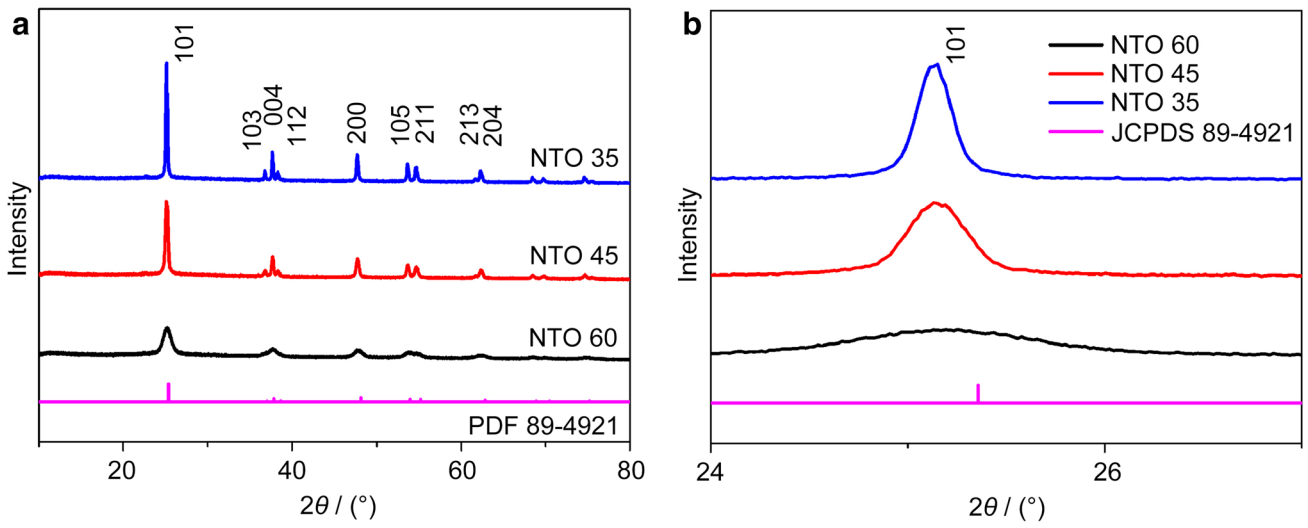

Fig. 1 **a** XRD patterns of NTO samples; **b** magnification of (101) area in **a**

full width at half-maximum of XRD patterns. The crystallite size was estimated from the (101) peak of XRD patterns using the Scherrer's equation (Eq. 1):

$$d = K\lambda/(\beta \cos\theta) \quad (1)$$

where d is the mean size of the crystalline domains, K is the dimensionless shape factor, with a typical value of ~ 0.9, λ is the X-ray wavelength, β is the line broadening at half the maximum intensity, and θ is the Bragg angle.

The higher ethanol concentration during the synthesis process gave the smaller crystallite size of 6.16, 24.74 and 42.52 nm for sample NTO 60, NTO 45 and NTO 35, respectively. The controlled release of water by acetic acid took part in the particle growing of the crystal. The particle size was directly affected by the amount of water molecules that dissolve the precursor [42]. The use of alcohol was proven to provide NTO with a small particle size [43].

The nanostructure of NTO was investigated using TEM, as presented in Fig. 2a–c. The nanoparticle size increased with the increasing addition of acetic acid. The water-controlled release solvothermal method using acetic acid provides water molecules to accelerate the dissolution of metal ions, and larger-sized particles can be formed along

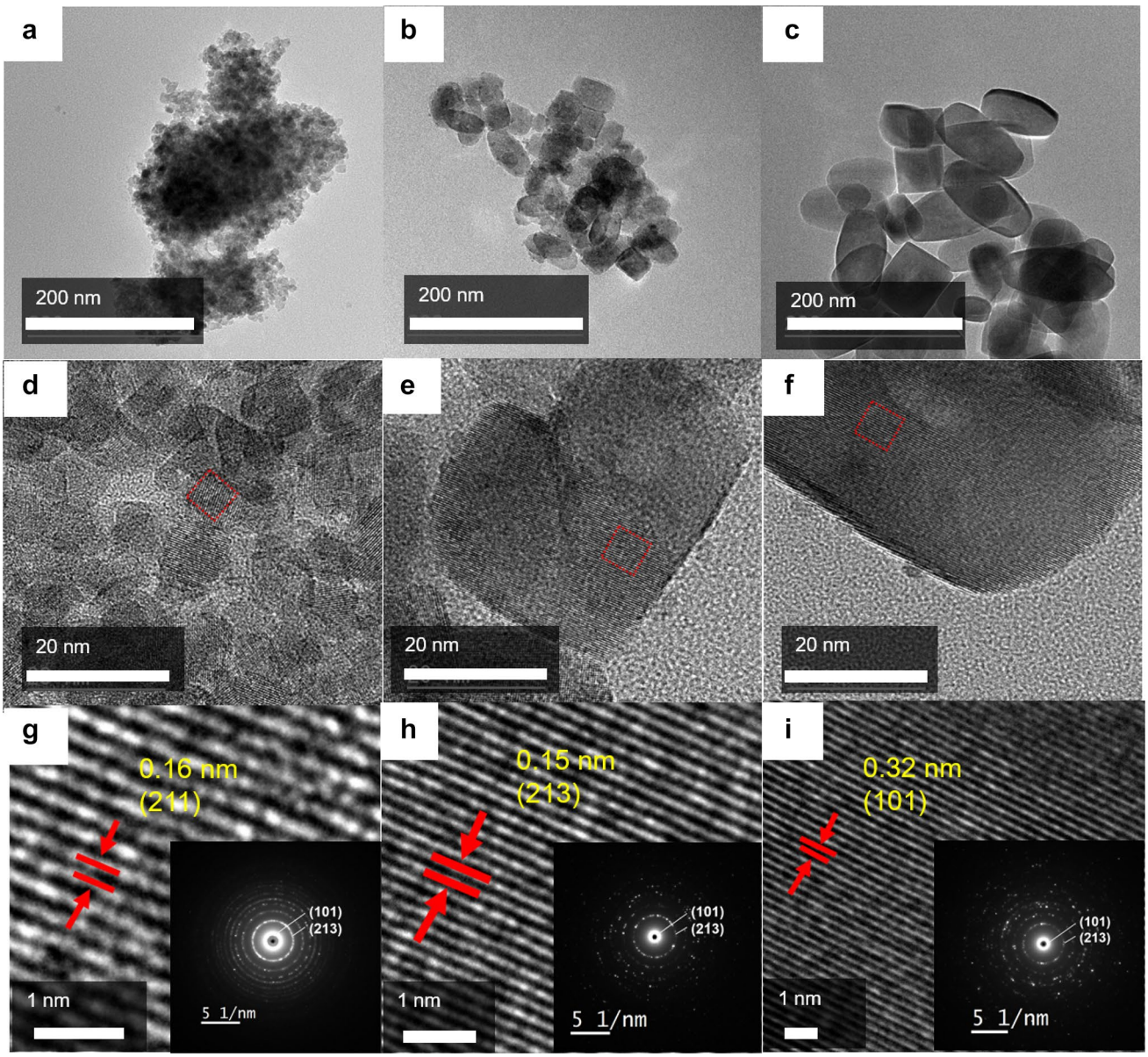

Fig. 2 **a–c** TEM images and **d–f** HR-TEM images of NTO 60, NTO 45 and NTO 35, respectively; **g–i** lattice fringes of the corresponding areas in **d–f**, respectively. The inset images in **g–i** are the SAED patterns of NTO 60, NTO 45, and NTO 35, respectively

Table 1 Specific surface area, surface Nb composition, and bandgap energy of the NTO samples

CH_3CH_2OH/mL	CH_3OOH/mL	Samples denotation	Specific surface area/(m^2 g^{-1})	Surface composition of Nb/at%	Band gap energy/eV
60	0	NTO 60	197	5.03	3.2
45	15	NTO 45	168	5.36	3.2
35	25	NTO 35	60	5.19	3.2

with the particle growth. The use of ethanol, however, produces the fine particle size as can be seen in the sample NTO 60. Among all the samples, the particle sizes of the sample synthesized using ethanol solvent showed the smallest value of ~ 1–10 nm, corresponding to the scale predicted by the calculation derived from the broadening peaks of XRD measurement (Fig. 2d–f). The biggest particle size was obtained in NTO 35 with a size between 40 and 50 nm. The interplanar distances of 0.16, 0.15, and 0.32 nm for all samples matched well to the (211), (213) and (101) facets, respectively, agreeing with the XRD results for sample NTO 60, NTO 45 and NTO 35, respectively. The corresponding SAED patterns presented in the insets of Fig. 2g–i showed that the index matched to (211), (213) and (101) facets for all three polycrystalline samples.

The specific surface areas of all NTO samples are presented in Table 1. The specific surface area was obtained from BET method using the nitrogen adsorption measurement. The UV–Vis transmittance spectra and NIR shielding property of the NTO samples are presented in Fig. 3. The NTO films were prepared by dispersing NTO powders in collodion and casting the solution on the glass surface. The transmittance at 1000 nm was kept above 80% for all samples. The thicknesses of the films were uniform, as shown by the few differences in transmittance among samples. The average transmittance in the visible region between 350 and 800 nm was observed as 84%, 77% and 75% for NTO 60, 45 and 35, respectively. The NTO 60 showed just a few NIR shielding activity while samples NTO 45 and NTO 35 showed distinct NIR shielding properties. The NIR shielding activity of NTO 45 was the highest and up to 20% higher than that of NTO 60. These results showed that the NIR shielding property of NTO nanoparticles should be beneficial for the improvement of its multifunctional property.

The photocatalytic deNO_x activities of the NTO powder samples are summarized in Fig. 4. The deNO_x activities of the samples were compared to that of a standard photocatalyst P-25 titania (Degussa AG). All NTO samples showed the deNO_x activity, while the highest activity was given by NTO 60 of 28%. The reason for the lower photocatalytic activity for all NTO samples compared to that of P-25 titania was due to the existence of Ti^{3+}, as a result of the reduction during the synthesis process. The Ti^{3+} species could act as a recombination site for the excited holes and electrons [40]. Even so, Ti^{3+}

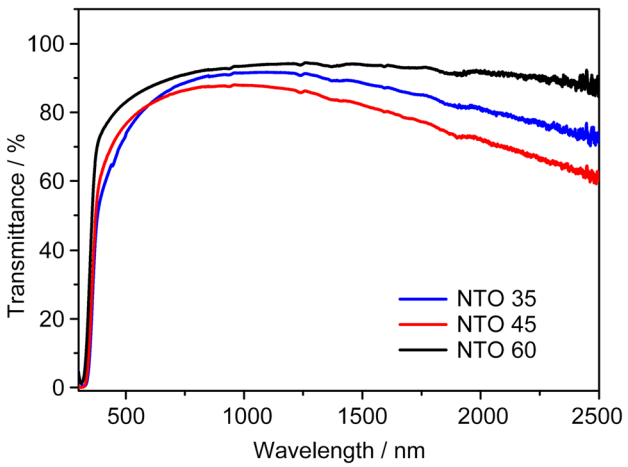

Fig. 3 Transmittance spectra/NIR shielding abilities of NTO samples

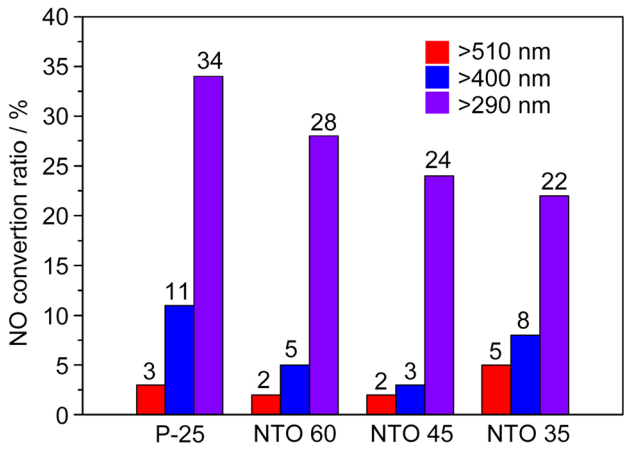

Fig. 4 DeNO_x photocatalytic activities of NTO powder samples

species also gave the advantages of NIR shielding and photocatalysis and therefore would be suitable for the next step of the multifunctionality thin films.

Figure 5 presents the energy band gaps of NTO samples which were the same at 3.2 eV. The estimation of the band gap was carried using Tauc plot of Kubelka–Munk equation (see Eq. 2):

$$(F(R)h\nu)^{1/n} = (\alpha h\nu)^{1/n} = A\left(h\nu - E_g\right) \quad (2)$$

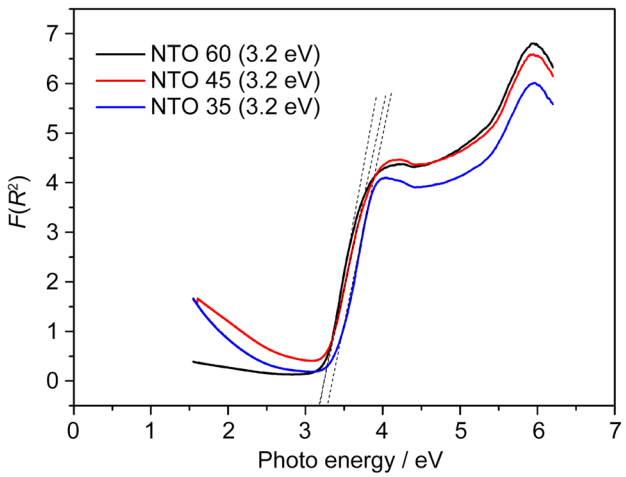

Fig. 5 Bandgap energies of the NTO samples

where $F(R)$ is Kubelka–Munk function, h is Planck's constant, ν is the frequency of vibration, R is the diffused reflectance of the samples, α is the absorption coefficient, A is the proportional constant and E_g is the band gap with direct allowed transition assumption ($n = 1/2$).

NTO was known to provide an impurity band that overlapped with the conduction band of anatase. The doping does not alter the band distribution but only fill the conduction band. The substituted Nb atoms were ionized and provided electrons into the hybridized conduction band consisted of Ti 3*d* and Nb 3*d* states [44]. The emission photon energies are near to the bandgap energy at 3.2 eV, and the band gap energy of NTO showed that the photocatalytic activity of NTO would be suitable to utilize UV irradiation.

The surface chemical composition and valence states of each element in NTO are presented in Fig. 6. The characteristic peaks of Ti $2p_{1/2}$ and Ti $2p_{3/2}$ were observed from all NTO samples. For samples NTO 60 and NTO 45, the corresponding peaks of Ti^{4+} ions were observed at the binding energy of 458.9 and 459.8 eV, respectively. A minor shift to the lower binding energy at 458.4 eV was observed for sample NTO 35 that could be the indication for the existence of Ti^{3+}. The binding energy of 458.4 eV was, however, still within the corresponding peak range of Ti^{4+} ions [44]. The Nb $3d_{3/2}$ and Nb $3d_{5/2}$ peaks are presented in Fig. 6b. For samples NTO 60 and NTO 45, pronounced Nb^{5+} peaks were observed at 207.1 and 207.3 eV, respectively. For sample NTO 35, Nb^{4+} was indicated at the binding energy of 206.8 eV [43–46]. The XPS analysis provided the surface composition of NTO samples. The surface composition of Nb doping for all NTO samples was maintained at ~ 5%, as summarized in Table 1.

3.2 Thermochromic performance of coexistent and double-sided VO_2/NTO films

To examine the multifunctionality of two types of coatings: double-sided and coexistence films, each NTO and VO_2(M) were dispersed as a double-sided film so that they were on the opposite side of the borosilicate glass. VO_2(M) and NTO were prepared at the same weight. The transmittance spectra of the VO_2/NTO double-sided coating are presented in Fig. 7a. The transmittance showed that the NIR shielding properties measured at room temperature could not be observed for all samples. It could be that the addition of VO_2 in the mixture disturbed and lowered the intensity of the NIR shielding property of NTO. It was reported that the NIR shielding effect could be reduced in the composite thin films [47]. The transmittances of VO_2/NTO samples were all higher than that of the VO_2(M) reference film even at the

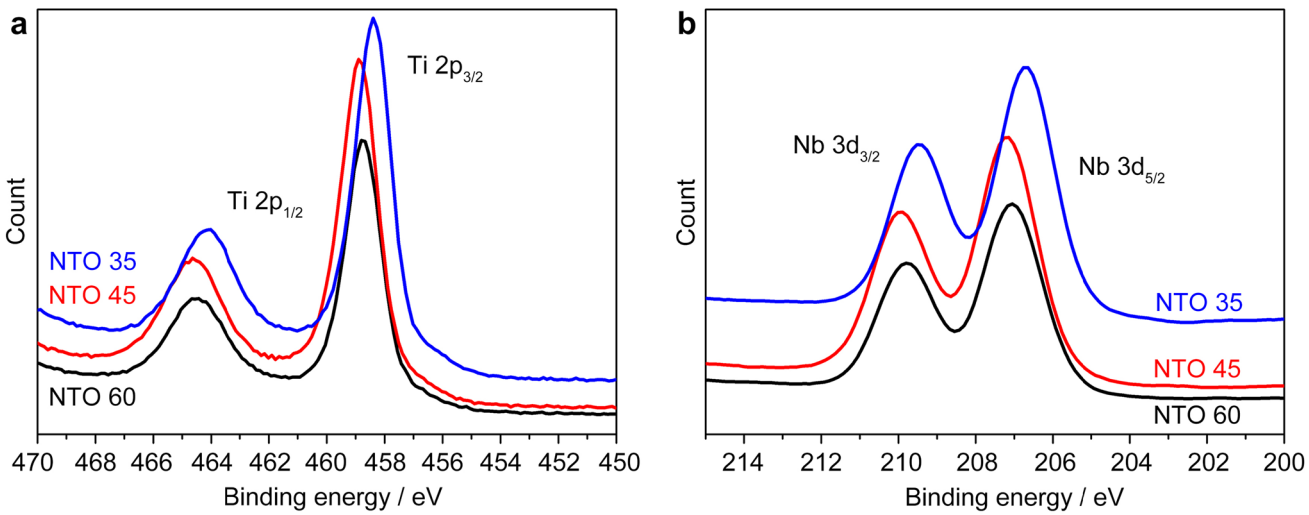

Fig. 6 XPS spectra of NTO samples: **a** Ti 2p; **b** Nb 3d

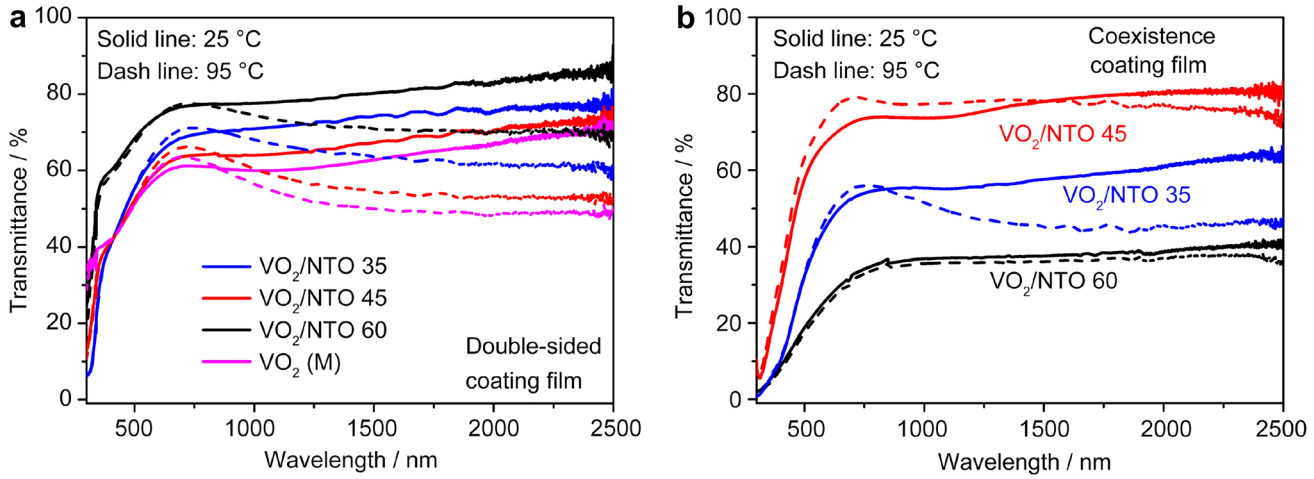

Fig. 7 Transmittance spectra of VO_2/NTO samples in **a** double-side and **b** coexistence coating films at 25 °C (solid line) and 95 °C (dashed line)

visible wavelength region. Using collodion of 50 µmol L^{-1}, the transmittances were kept above 60% for all samples. The $\Delta T_{1500\ nm}$ for the double-side coating films were 9%, 13%, and 16% for samples NTO 60, NTO 45 and NTO 35, respectively, comparable to $\Delta T_{1500\ nm}$ of VO_2(M) at 13%.

A more commonly used mode of multifunctionality is the coexistence coating in which the combination of materials is cast on the same surface of the glass. The UV–Vis–NIR transmittance of the coexistence coating films after removal of collodion by heating under air at 200 °C is presented in Fig. 7b. The coexistence coating films were lower in quality compared to the double-side coating films. The $\Delta T_{1500\ nm}$ for the coexistence coating films were 1%, 0, and 12% for samples NTO 60, NTO 45 and NTO 35, respectively. Only sample VO_2/NTO 45 maintained the thermochromic performance. The poor quality of the coexistence films decreased not just for $\Delta T_{1500\ nm}$ but also for the transmittance in the visible range wavelength. These results showed that the utilization of pristine VO_2 was better in the separately double-sided coating films compared to the combination of NTO in the coexistence coating films.

3.3 Thermochromic performance of coexistent and double-sided F–VO_2/NTO coating films

The properties of F–VO_2 were described in a previous report [41]. F–VO_2 reduced the critical temperature of MST up to 48 °C. The XRD pattern of F–VO_2 showed matching peaks to the monoclinic VO_2 phase with reference JCPDS 44-0252 (Fig. 8). The TEM, HR-TEM, and SAED images of the prepared F–VO_2 sample are presented in Fig. 9. The TEM images of F–VO_2 in Fig. 9a showed that the morphology of the F–VO_2 particle was an irregular sphere. Further, the HR-TEM image in Fig. 9b, c showed that the lattice fringes were matched to the distance between planes of atoms

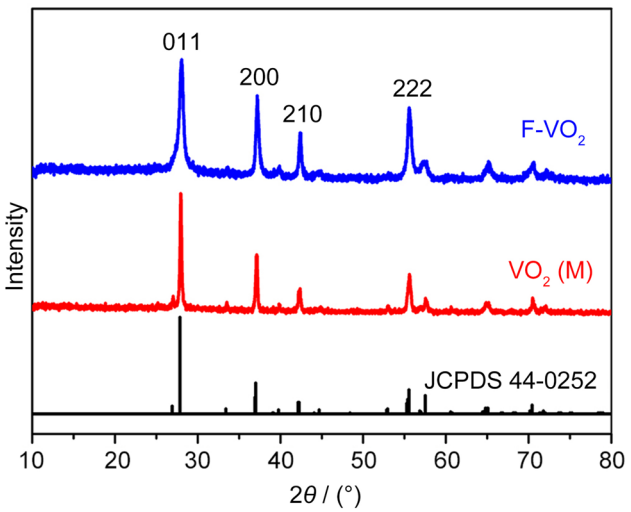

Fig. 8 XRD patterns of F–VO_2 and VO_2(M), together with the reference JCPDS 44-0252

[*d* spacing (012) of VO_2(M)]. There is also a presence of a 7.5 nm thickness of the fluorine-doped surface layer on the particles. This layer could be involved in the increasing thermochromic and photocatalytic activity, as explained below. The SAED pattern in Fig. 9d showed that the index matched to the (100) and (210) facets of F–VO_2.

The transmittance of double-sided and coexistence coating films of F–VO_2/NTO samples is presented in Fig. 10. The F–VO_2/NTO samples of both coexistence and double-sided coating films were better in transmittance than that of VO_2/NTO. The coating films of F–VO_2 were indeed proven to enhance the poor visible light transition due to the strong absorption of visible wavelengths. The fluorine doping adjusted the transmittance by adjusting the optical band gap of VO_2 [48].

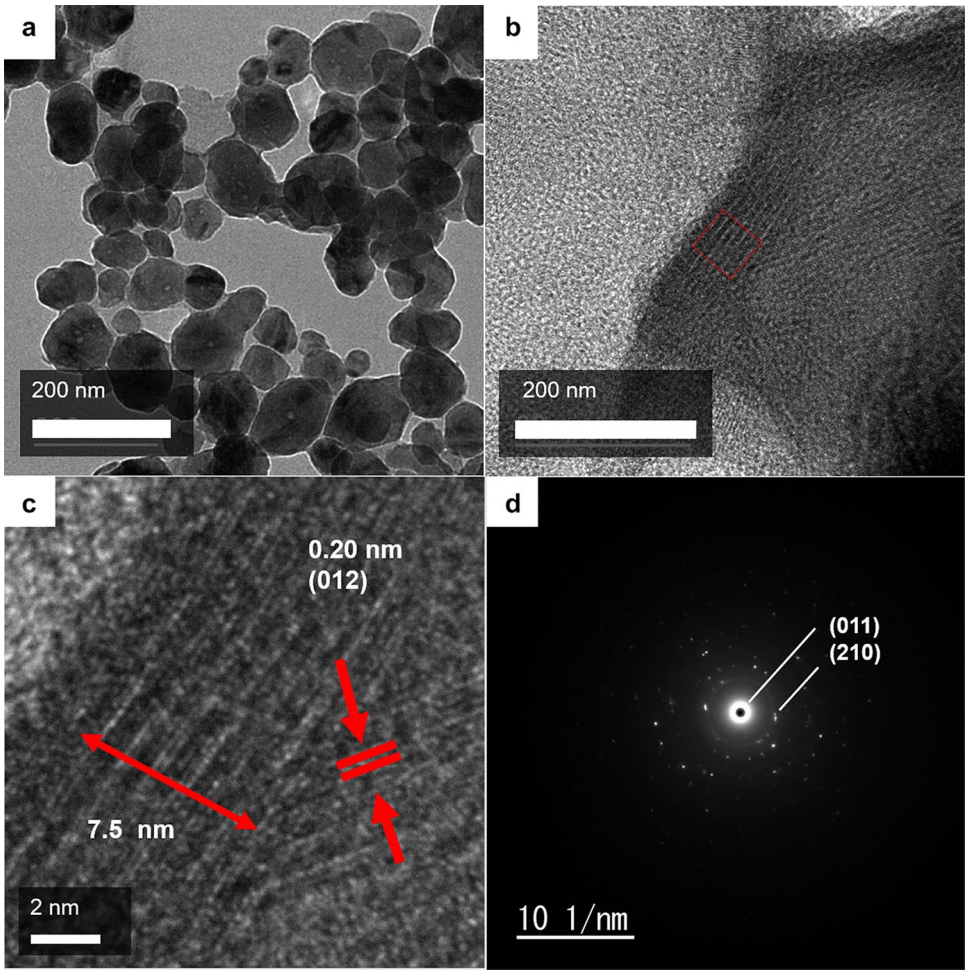

Fig. 9 **a** TEM, **b** HR-TEM, **c** Lattice fringes from the selected area in **b**, and **d** SAED pattern of the F–VO_2 sample

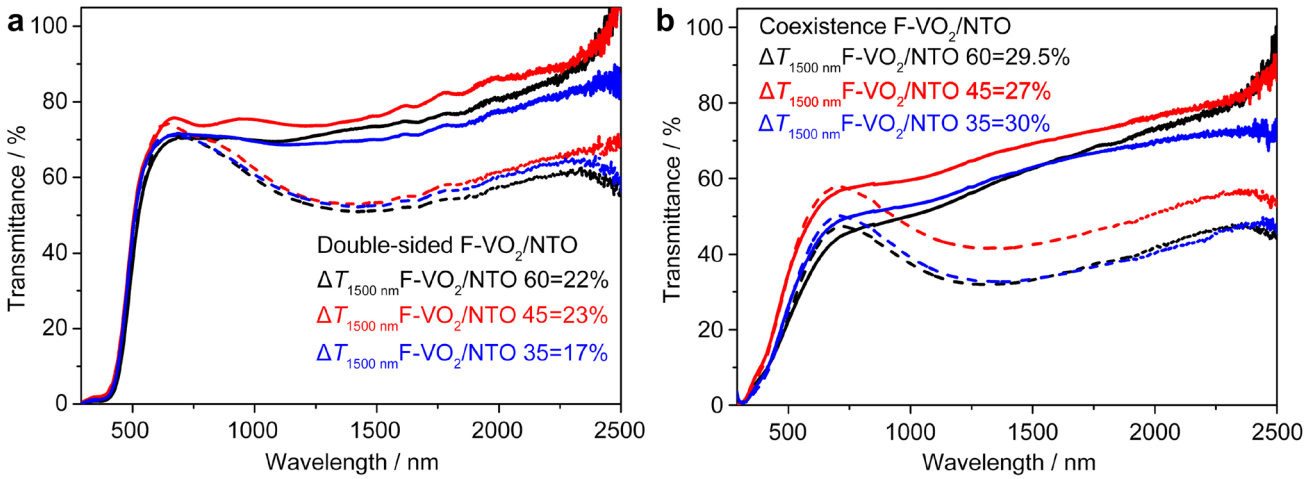

Fig. 10 Transmittance of F–VO_2/NTO with **a** double-side and **b** coexistence coating films at 25 °C (solid line) and 95 °C (dashed line)

The effect of the room temperature NIR shielding of NTO to the transmittance was not significant to both samples for VO_2/NTO and F–VO_2/NTO. The transmittance of both samples at visible range wavelengths showed that the double-sided films provided higher transmittance compared to those of the coexistence coating films. However, the thermochromic performance was higher for coexistence films. For the double-sided coating films, the values of $\Delta T_{1500\ nm}$

were 22%, 23%, and 17% for samples NTO 60, NTO 45 and NTO 35, respectively (Fig. 10a). Meanwhile the value of $\Delta T_{1500\,nm}$ for the coexistence coating films were 29.5%, 27%, and 30% for samples NTO 60, NTO 45, and NTO 35, respectively (Fig. 10b). The coexistence coating films of F–VO_2/NTO showed the higher transmittance and multifunctionality than those of VO_2/NTO coating films. The best thermochromic performance was given by sample F–VO_2/NTO 35 with $\Delta T_{1500\,nm}$ of 30%, and F–VO_2/NTO 60 showed a small difference value of 29.5%.

3.4 $DeNO_x$ activities of coexistent and double-sided coating films

The photocatalytic NO_x decomposition activities of the obtained F–VO_2/NTO, VO_2/NTO and pristine VO_2 coating films at $\lambda > 290$ nm under Hg lamp irradiation are summarized in Fig. 11. As the bandgap of NTO was at 3.2 eV, the photocatalysis was performed in the UV wavelength area with the light filter set to $\lambda > 290$ nm. The NO conversion ratios for the double-sided coating films were 26%, 22%, and 20% at $\lambda > 290$ nm, and the NO conversion ratios for the coexistence coating films were 40%, 35%, and 33% for samples F–VO_2/NTO 60, F–VO_2/NTO 45, and F–VO_2/NTO 35, respectively. This result showed that the fluorine doping played a beneficial effect on the behavior of the coating films compared to the separately used F–VO_2 and NTO in the double-sided coating films. The coexistence films of F–VO_2/NTO showed appropriateness to be used as a multifunctional material. On double-sided F–VO_2/NTO coating films, the sample consisted of NTO 60 possessed the highest $deNO_x$ activity in all the synthesized samples. The result was consistent with the fine particle size and high specific surface area of NTO 60 that was more appropriate to give a high photocatalysis performance.

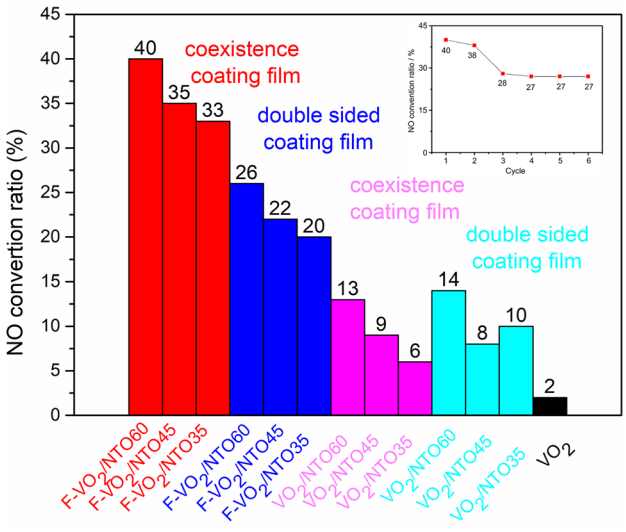

Fig. 11 $DeNO_x$ activity of F–VO_2/NTO compared to those of VO_2/NTO and pristine VO_2 samples with coexistence and double-sided coating films at $\lambda > 290$ nm under Hg lamp irradiation. The insert indicates the photocatalytic stability of F–VO_2/NTO 60 with a coexistence coating film irradiated at $\lambda > 290$ nm under the Hg lamp

The NTO with the anatase structure possessed a bandgap energy of 3.2 eV. Meanwhile VO_2 had the small bandgap energy of 0.7 eV, which was not suitable for photocatalysis due to the closeness of the conducting properties of VO_2 [49], although a report showed that vanadium oxides including VO_2(M) could be potential for photocatalytic hydrogen production [50]. Even at the dielectric films, for some composites such as TiO_2/VO_2, the band edge line alignment is predicted to be within the band gap energy of TiO_2. The conduction band offset for VO_2 with the conduction band offset value of the TiO_2 interface is ~ 0.6 eV [51]. The improved $deNO_x$ activity for the F–VO_2/NTO samples could be due to the fluorine anion doping in the surface of VO_2, which might interact to the surface of NTO in the polymer matrix during mixing. As shown in the HR-TEM image of F–VO_2 (Fig. 9c), there was a layer observed at the outer side of the F–VO_2 surface with a thickness of 7.5 nm, which could be the active layer that interacted with NTO. Fluorine in the surface could interact with the surface of NTO while maintaining its thermochromic performance. It was reported that fluorine could provide Ti–F bonds that resulted in the generation of free OH radicals that improved the photocatalytic activity [52–55].

Contrary to the result of F–VO_2/NTO samples, for VO_2/NTO samples, the double-sided films gave a better result than that of the coexistence coating films. The photocatalytic activities of VO_2/NTO coating films were lower than those of F–VO_2/NTO with both coexistence and double-sided films, as well as comparing to the $deNO_x$ activity of powder NTO. This low activity could be related to the various processes going through such as the addition of nitrocellulose, drying, and heating of coating films at 200 °C under air. Such processes could degrade the quality of NTO. Sample VO_2/NTO 60 gave the best $deNO_x$ activity among VO_2/NTO samples, indicating the role of the fine particle size and high specific surface area for better photocatalytic activity.

To evaluate the photocatalytic stability, multi-cycles of $deNO_x$ activity was measured for sample F–VO_2/NTO 60 with a coexistence coating film irradiated at $\lambda > 290$ nm using the mercury lamp (Fig. 11). The result showed that after testing for three runs, the $deNO_x$ photocatalytic activity of the sample was stabilized at 27% which did not change up to six cycles, implying its good photo stability. Although the $deNO_x$ activity decreased, the value of 27% was still higher than those of double-sided F–VO_2/NTO and all VO_2/NTO coating film samples.

4 Conclusion

Multifunctional coatings of VO_2/NTO and F–VO_2/NTO were obtained from the physical mixing of nanoparticles prepared using a facile solvothermal process. Coexistence and double-sided coating films were prepared to determine whether a single effect of each component or multifunctional effect would be more suitable to the property of the composites. All the coating films possessed the thermochromic property and deNO_x activity, suggesting the appropriateness for a multifunctional coating. The F–VO_2/NTO coating films possessed better multifunctional properties than those of VO_2/NTO coating films. F–VO_2/NTO samples provided the better transmittance and higher thermochromic property than those of VO_2/NTO, due to the fluorine doping effect of reducing the critical temperature of the phase transition in VO_2(M), as well as modifying the bandgap to adjust the transmittance at the visible range wavelength. The deNO_x activity was enhanced for F–VO_2/NTO in the coexistence coating films compared to the double-sided coating films. The F–VO_2/NTO showed the better appropriateness for multifunctionality than that of VO_2/NTO. The highest deNO_x activity in all the synthesized samples was given by F–VO_2/NTO 60 with $\Delta T_{1500\,nm}$ up to 29.5% and deNO_x activity up to 40% at $\lambda > 290$ nm under mercury lamp irradiation. Samples F–VO_2/NTO and VO_2/NTO containing NTO 60 showed a better photocatalytic activity than those of NTO 45 and NTO 35. Sample NTO 60 has the smallest particle size and the highest specific surface area as a result of the solvothermal synthesis process, suggesting the importance of these factors in the photocatalysis and the multifunctionality properties enhancement.

Acknowledgements This research was financially supported by the JSPS KAKENHI [Grant-in-Aid for Scientific Research on Innovative Areas "Mixed Anion" (Grant No. 16H06439)]; the Cooperative Research Program of "Network Joint Research Center for Materials and Devices"; and the Dynamic Alliance for Open Innovations Bridging Human, Environment, and Materials.

References

1. Cao X, Dai X, Liu J. Building energy-consumption status worldwide and the state-of-the-art technologies for zero-energy buildings during the past decade. Energy Build. 2016;128:198.
2. Chen Y, Zeng X, Zhou Y, Li R, Yao H, Cao X, Jin P. Core-shell structured Cs_xWO_3@ZnO with excellent stability and high performance on near-infrared shielding. Ceram Int. 2018;44(3):2738.
3. Yin S, Asakura Y. Recent research progress on mixed valence state tungsten based materials. Tungsten. 2019;1(1):5.
4. Yin S, Riapanitra A, Asakura Y. Nanomaterials for infrared shielding smart coatings. Funct Mater Lett. 2018;11(5):1830004.
5. Ghosh A, Norton B. Advances in switchable and highly insulating autonomous (self-powered) glazing systems for adaptive low energy buildings. Renew Energy. 2018;126:1003.
6. Granqvist CG. Electrochromics for smart windows: oxide-based thin films and devices. Thin Solid Films. 2014;564:1.
7. Granqvist CG, Green S, Niklasson GA, Mlyuka NR, von Kræmer S, Georén P. Advances in chromogenic materials and devices. Thin Solid Films. 2010;518(11):3046.
8. Liu G, Sun C, Yan X, Cheng L, Chen ZG, Wang X, Wang L, Smith SC, Lu G, Cheng HM. Iodine doped anatase TiO_2 photocatalyst with ultra-long visible light response: correlation between geometric/electronic structures and mechanisms. J Mater Chem. 2009;19(18):2822.
9. Riapanitra A, Asakura Y, Yin S. One-step hydrothermal synthesis and thermochromic properties of chlorine-doped VO_2(M) for smart window application. Funct Mater Lett. 2019;12:1951008.
10. Singh S, Sharma V, Sachdev K. Investigation of effect of doping concentration in Nb-doped TiO_2 thin films for TCO applications. J Mater Sci. 2017;52(19):11580.
11. Morin FJ. Oxides which show a metal-to-insulator transition at the neel temperature. Phys Rev Lett. 1959;3(1):34.
12. Granqvist CG. Electrochromics and thermochromics: towards a new paradigm for energy efficient buildings. Mater Today Proc. 2016;3:S2.
13. Granqvist CG. Recent progress in thermochromics and electrochromics: a brief survey. Thin Solid Films. 2016;614(Part B):90.
14. Burkhardt W, Christmann T, Franke S, Kriegseis W, Meister D, Meyer BK, Niessner W, Schalch D, Scharmann A. Tungsten and fluorine co-doping of VO_2 films. Thin Solid Films. 2002;402(1–2):226.
15. Burkhardt W, Christmann T, Meyer BK, Niessner W, Schalch D, Scharmann A. W- and F-doped VO_2 films studied by photoelectron spectrometry. Thin Solid Films. 1999;345(2):229.
16. Li Y, Wu X, Li J, Wang K, Zhang G. Z-scheme g-C_3N_4@Cs_xWO_3 heterostructure as smart window coating for UV isolating, Vis penetrating, NIR shielding and full spectrum photocatalytic decomposing VOCs. Appl Catal B. 2018;229:218.
17. Banerjee S, Dionysiou DD, Pillai SC. Self-cleaning applications of TiO_2 by photo-induced hydrophilicity and photocatalysis. Appl Catal B. 2015;176–177:396.
18. Fujishima A, Honda K. Electrochemical photolysis of water at a semiconductor electrode. Nature. 1972;238:37.
19. Komatsuda S, Asakura Y, Vequizo JJM, Yamakata A, Yin S. Enhanced photocatalytic NO_x decomposition of visible-light responsive F-TiO_2/(N, C)-TiO_2 by charge transfer between F-TiO_2 and (N, C)-TiO_2 through their doping levels. Appl Catal B. 2018;238:358.
20. Wu X, Yin S, Dong Q, Guo C, Kimura T, Matsushita JI, Sato T. Photocatalytic properties of Nd and C codoped TiO_2 with the whole range of visible light absorption. J Phys Chem C. 2013;117(16):8345.
21. Liu T, Liu B, Wang J, Yang L, Ma X, Li H, Zhang Y, Yin S, Sato T, Sekino T, Wang Y. Smart window coating based on F-TiO_2-K_xWO_3 nanocomposites with heat shielding, ultraviolet isolating, hydrophilic and photocatalytic performance. Sci Rep. 2016;6:27373.
22. Yin S, Aita Y, Komatsu M, Wang J, Tang Q, Sato T. Synthesis of excellent visible-light responsive TiO_2-N photocatalyst by a homogeneous precipitation-solvothermal process. J Mater Chem. 2005;15(6):674.
23. Jiang C, Wu Z, Xiao S, Ma Z, Liu L, Fu RKY, Chu PK, Lin H, Pan F. Structural and optoelectrical properties of Nb–TiO_2 films fabricated by low-energy magnetron sputtering and post-annealing. Surf Coat Technol. 2019;365:10.
24. Eguchi R, Takekuma Y, Ochiai T, Nagata M. Improving interfacial charge-transfer transitions in Nb-Doped TiO_2 electrodes with 7,7,8,8-tetracyanoquinodimethane. Catalysts. 2018;8(9):367.

25. Singh S, Sharma V, Asokan K, Sachdev K. NTO/Ag/NTO multilayer transparent conducting electrodes for photovoltaic applications tuned by low energy ion implantation. Sol Energy. 2018;173:651.
26. Emeline AV, Furubayashi Y, Zhang X, Jin M, Murakami T, Fujishima A. Photoelectrochemical behavior of Nb-doped TiO_2 electrodes. J Phys Chem B. 2005;109(51):24441.
27. Adomnitei C, Tascu S, Luca D, Dobromir M, Girtan M, Mardare D. Nb-doped TiO_2 thin films as photocatalytic materials. Bull Mater Sci. 2015;38(5):1259.
28. Kong L, Wang C, Zheng H, Zhang X, Liu Y. Defect-induced yellow color in Nb-doped TiO_2 and its impact on visible-light photocatalysis. J Phys Chem C. 2015;119(29):16623.
29. Qian X, Wang N, Li Y, Zhang J, Xu Z, Long Y. Bioinspired multifunctional vanadium dioxide: improved thermochromism and hydrophobicity. Langmuir. 2014;30(35):10766.
30. Mihailescu CN, Symeou E, Svoukis E, Negrea RF, Ghica C, Teodorescu V, Tanase LC, Negrila C, Giapintzakis J. Ambiguous Role of Growth-Induced Defects on the Semiconductor-to-Metal Characteristics in Epitaxial VO_2/TiO_2 Thin Films. ACS Appl Mater Interfaces. 2018;10(16):14132.
31. Im JS, Anoop G, Sohn MK, Kang DJ, Jeong SY, Lee S, Jo JY. Oxygen stoichiometry controlled sharp insulator-metal transition in highly oriented VO_2/TiO_2 thin films. Curr Appl Phys. 2018;18(6):652.
32. Top I, Binions R, Warwick MEA, Dunnill CW, Holdynski M, Abrahams I. VO_2/TiO_2 bilayer films for energy efficient windows with multifunctional properties. J Mater Chem C. 2018;6(16):4485.
33. Powell MJ, Quesada-Cabrera R, Taylor A, Teixeira D, Papakonstantinou I, Palgrave RG, Sankar G, Parkin IP. Intelligent multifunctional $VO_2/SiO_2/TiO_2$ coatings for self-cleaning, energy-saving window panels. Chem Mater. 2016;28(5):1369.
34. Mlyuka NR, Niklasson GA, Granqvist CG. Thermochromic multilayer films of VO_2 and TiO_2 with enhanced transmittance. Sol Energy Mater Sol Cells. 2009;93(9):1685.
35. Miller MJ, Wang J. Multilayer ITO/VO_2/TiO_2 thin films for control of solar and thermal spectra. Sol Energy Mater Sol Cells. 2016;154:88.
36. Yin S. Creation of advanced optical responsive functionality of ceramics by green processes. J Ceram Soc Jpn. 2015;123(1441):823.
37. Li D, Li M, Pan J, Luo Y, Wu H, Zhang Y, Li G. Hydrothermal Synthesis of Mo-Doped VO_2/TiO_2 Composite Nanocrystals with Enhanced Thermochromic Performance. ACS Appl Mater Interfaces. 2014;6(9):6555.
38. Salamati M, Kamyabjou G, Mohamadi M, Taghizade K, Kowsari E. Preparation of TiO_2@W-VO_2 thermochromic thin film for the application of energy efficient smart windows and energy modeling studies of the produced glass. Constr Build Mater. 2019;218:477.
39. Zhao Z, Fan J, Chang H, Asakura Y, Yin S. Recent progress on mixed-anion type visible-light induced photocatalysts. Sci China Technol Sci. 2017;60(10):1447.
40. Asakura Y, Anada Y, Hamanaka R, Sato T, Katsumata KI, Wu X, Yin S. Multifunctionality in coating films including Nb-doped TiO_2 and Cs_xWO_3: near infrared shielding and photocatalytic properties. Nanotechnology. 2018;29(22):224001.
41. Riapanitra A, Asakura Y, Cao W, Noda Y, Yin S. Supercritical temperature synthesis of fluorine-doped VO_2(M) nanoparticle with improved thermochromic property. Nanotechnology. 2018;29(24):244005.
42. Wojnarowicz J, Chudoba T, Malka I, Gierlotka S, Dworakowska S, Lojkowski W. Size control mechanism of ZnO nanoparticles obtained in microwave solvothermal synthesis. Nanotechnology. 2018;29(6):065601.
43. Liu Y, Szeifert JM, Feckl JM, Mandlmeier B, Rathousky J, Hayden O, Fattakhova-Rohlfing D, Bein T. Niobium-doped titania nanoparticles: synthesis and assembly into mesoporous films and electrical conductivity. ACS Nano. 2010;4(9):5373.
44. Hitosugi T, Kamisaka H, Yamashita K, Nogawa H, Furubayashi Y, Nakao S, Yamada N, Chikamatsu A, Kumigashira H, Oshima M, Hirose Y, Shimada T, Hasegawa T. Electronic band structure of transparent conductor: Nb-doped anatase TiO_2. Appl Phys Express. 2008;1(11):111203.
45. Atashbar MZ, Sun HT, Gong B, Wlodarski W, Lamb R. XPS study of Nb-doped oxygen sensing TiO_2 thin films prepared by sol-gel method. Thin Solid Films. 1998;326(1–2):238.
46. Daccà A, Gemme G, Mattera L, Parodi R. XPS analysis of the surface composition of niobium for superconducting RF cavities. Appl Surf Sci. 1998;126(3–4):219.
47. Manole AV, Dobromir M, Gîrtan M, Mallet R, Rusu G, Luca D. Optical properties of Nb-doped TiO_2 thin films prepared by sol–gel method. Ceram Int. 2013;39(5):4771.
48. Dai L, Chen S, Liu J, Gao Y, Zhou J, Chen Z, Cao C, Luo H, Kanehira M. F-doped VO_2 nanoparticles for thermochromic energy-saving foils with modified color and enhanced solar-heat shielding ability. Phys Chem Chem Phys. 2013;15(28):11723.
49. Goodenough JB. The two components of the crystallographic transition in VO_2. J Solid State Chem. 1971;3(4):490.
50. Shen TFR, Lai MH, Yang TCK, Fu IP, Liang NY, Chen WT. Photocatalytic production of hydrogen by vanadium oxides under visible light irradiation. J Taiwan Inst Chem Eng. 2012;43(1):95.
51. Zhang Z, Chen J, Guo Y, Robertson J. Band alignment calculation of dielectric films on VO_2. Microelectron Eng. 2019;216:111057.
52. Liu G, He F, Zhang J, Li L, Li F, Chen L, Huang Y. Yolk–shell structured Fe_3O_4@C@F-TiO_2 microspheres with surface fluorinated as recyclable visible-light driven photocatalysts. Appl Catal B. 2014;150–151:515.
53. Yang HG, Sun CH, Qiao SZ, Zou J, Liu G, Smith SC, Cheng HM, Lu GQ. Anatase TiO_2 single crystals with a large percentage of reactive facets. Nature. 2008;453:638.
54. Yu J, Wang W, Cheng B, Su BL. Enhancement of photocatalytic activity of mesoporous TiO_2 powders by hydrothermal surface fluorination treatment. J Phys Chem C. 2009;113(16):6743.
55. Chen S, Yang Y, Liu W. Preparation, characterization and activity evaluation of TiN/F-TiO_2 photocatalyst. J Hazard Mater. 2011;186(2–3):1560.

Dr. Anung Riapanitra is currently working as a full-time lecturer at the Department of Chemistry, Faculty of Mathematics and Natural Science Jenderal Soedirman University, Indonesia. He received his master's degree from the School of Chemistry, University of Tasmania by the funding from the Australian Partnership Scholarship Award. He received Indonesia Endowment Fund for Education (LPDP) Scholarship Award for doctoral degree study. He received his Ph.D. degree from the Department of Frontier Sciences for Advances Environment, Graduate School of Environmental Studies, Tohoku University in 2019, and received the Professional Director for Sustainable Environment Award among the selected graduates. He has authored and co-authored in some scientific publications such as *Angewandte Chemie International Edition*, *Applied Surface Science*, and *Nanotechnology*. His research mainly focuses on the preparation of the environmental response materials by liquid-phase processes such as the hydrothermal and solvothermal reaction.